Results in Physics 7 (2017) 2775–2790

Contents lists available at ScienceDirect

Results in Physics

journal homepage: www.journals.elsevier.com/results-in-physics

Numerical-experimental investigation of PE/EVA foam injection molded parts

Roberto Spina *

Dept. of Mechanics, Mathematics and Management (DMMM), Politecnico di Bari, Viale Japigia 182, 70126 Bari, Italy
CNR-IFN UOS Bari, Via Amendola 173, 70126 Bari, Italy

ARTICLE INFO

Article history:
Received 6 April 2017
Received in revised form 11 July 2017
Accepted 23 July 2017
Available online 3 August 2017

Keywords:
Foam injection molding
PE/EVA
Material characterization
DSC
Rheometer
Mechanical testing

ABSTRACT

The main objective of the presented work is to propose a robust framework to test foaming injection molded parts, with the aim of establishing a standard testing cycle for the evaluation of a new foam material based on numerical and experimental results. The research purpose is to assess parameters influencing several aspects, such as foam morphology and compression behavior, using useful suggestions from finite element analysis. The investigated polymeric blend consisted of a mixture of low density polyethylenes (LDPEs), a high-density polyethylene (HDPE), an ethylene-vinyl acetate (EVA) and an azodicarbonamide (ADC). The thermal, rheological and compression properties of the blend are fully described, as well as the numerical models and the parameters of the injection molding process.

Introduction

The fabrication of high quality polymer foamed parts is the result of a complex process in which material properties, process parameters and product design are accurately balanced and tuned-up. The behavior of a polymeric foam during processing and the performance of the final part are strongly determined by the material structure formed. During processing, a foam is normally subject to a complex thermo-mechanical evolution in which a gas is entrapped in a polymer matrix. The final microstructure influences the mechanical response of the manufactured part and its weight. The behavior of the foam material mainly depends on the properties of the solid matrix (polymer or blend type) and the characteristics of the cellular structure (cell size and distribution). The homogeneity of the cellular structure and the average cell size of the foam are two important factors to control in order to improve the mechanical properties of the foam, as reported in Notario et al. [1]. Several foaming techniques are available to achieve precise control over these factors. Consequently, cell dimensions may range from micrometers to centimeters, can be extremely mono-disperse or highly poly-disperse, and the gas/-foam volume ratio can vary over a wide range.

After reviewing the most updated research literature, the main trends are oriented towards the improvement of material microstructures and the prediction of the final part behavior under compression and/or impact tests. Cappetti et al. [2] used a design of experiment (DOE) technique to extract information to support numerical simulations. Compression tests at low and medium speeds were carried-out in conditions very close to the real conditions of use. The main relationships between the independent and dependent variables were identified using variance analysis, whereas the factorial analysis was used to discover those factors (called latents) influencing the product behavior in a non-evident manner. Yousef et al. [3] studied the potential use of artificial neural networks (ANNs) for polymer characterization. They used ANNs to model the tensile curves and mechanical properties of polyethylene and polypropylene, and relative blends. Research demonstrates that ANNs could be considered as an effective tool to reduce the cost of and time required for the experimental work. Demir et al. [4] investigated the effects of different fillers on the foam formation, density, mechanical properties, water uptake and morphology. The properties of the filled foams were compared with those of unfilled ones to evaluate the influence of the filler and better regulate the final foam behavior. The results pointed out that foam formation was promoted by a low filler concentration whereas a high filler concentration increased rigidity and strength. Pantani et al. [5] analyzed the foaming ability of a biodegradable polymer. A chemical blowing agent under high pres-

* Address: Dept. of Mechanics, Mathematics and Management (DMMM), Politecnico di Bari, Viale Japigia 182, 70126 Bari, Italy.
E-mail address: roberto.spina@poliba.it

http://dx.doi.org/10.1016/j.rinp.2017.07.054
2211-3797/

sure and temperature was used to produce parts with a cellular core and a compact solid skin. The effect of the blowing agent on density and morphology of foamed parts was important, registering a significant reduction in material density with respect to unfoamed parts. Kim et al. [6] proposed a method to determine whether a given combination of polymer and blowing agent under thermo-dynamic conditions could produce a foam of the desired quality. The method could give qualitative predictions and identify the upper bound on polymer foam cell densities. A specific formalism was used to represent voids in the mixture as particles occupying some space. These fictitious particles had no energy interactions with the true chemical species, only contributing to translational entropy. Arencon et al. [7] analyzed the influence of density of polyolefin-based foams on fracture, correlating the fracture parameters with the cell morphology and evaluating the effect of the different chemical nature. The proposed methodology considered the presence of air and gave good predictions for polypropylene foams but inadequate results were achieved for low density polyethylene foams, probably due to the instability of the fracture tests. Kossa [8] suggested a novel design of a compression fixture to improve accuracy of experiments for foam material characterization. The main feature of this new device, easily attachable to a single column testing machine, was the application of an equi-biaxial compression load to the foam specimens. Chinesta et al. [9] implemented a numerical model of forming processes involving the flow of foams based on macroscopic and microscopic approaches. In this model, the macroscopic flow parameters relied on microscopic characteristics of the cellular structure such as porosity, size, shape and orientation of the cells, cellular wall properties, etc. The main advantage of this multi-scale representation was its application to several foaming processes independently of the material properties. The model was applied to compute the 2 D flow fronts. Maheo and Viot [10] studied an expanded foam constituted of large mesoscopic beads and microscopic cells. The effects of the mesoscopic heterogeneities in the foam at the scale of the beads on both the macroscopic and local behaviors were evaluated with a numerical approach, supported with uni-axial compression tests. An important result was that a foam gradually increasing in density allowed the impact energy to be absorbed without involving a plateau due to a too-large density difference between the layers. Banyay et al. [11] proposed a robust framework to simulate a unit cell of a foamed part with a real pore distribution acquired by fusing 2D images from a scanning electronic microscope with 3D images from an X-ray microtomography. The segmented and filtered images were converted into triangular surface mesh and the finite element model was calibrated with the experimental compression tests.

Several numerical models of the foam injection molding have been developed in the recent years. Zhang et al. [12] developed a non-isothermal model based on the two-phase model in foam process. A mathematical model was implemented by coupling heat transfer between multiphase flow and mold solid, based on a finite volume method to estimate the temperature, pressure and flow fields. This model proves to be a very useful tool to analyze the cel-

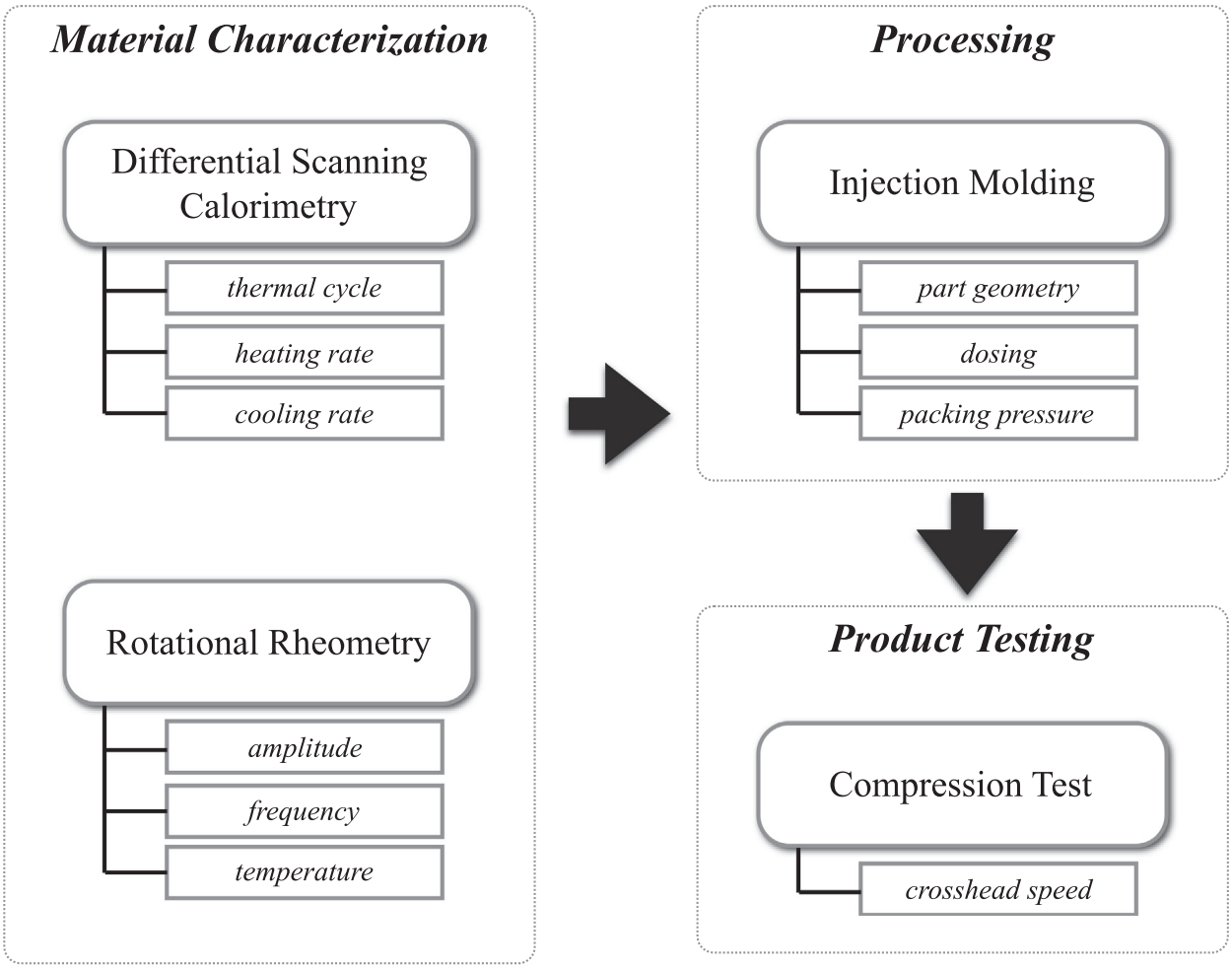

Fig. 1. Examination procedure flowchart.

lular morphology evolution process. Aloku and Yuan [13] investigated the computer simulations of foaming processes in extrusion flow to improve current understanding of viscoelasticity and bubble growth effects. One of the main results achieved was to discover that the bubble growth along the flow direction was affected by the viscoelasticity of polymer melt and the concentration of foaming agent, affecting the final foam density. Taki [14] implemented a simple kinetic model to investigate the creation and expansion of bubbles, consisting of a modified classical nucleation rate equation and a set of bubble growth rate equations. The model predicted the final number density of bubbles and bubble growth rate by determining, with one experiment, the two fitting parameters related to bubble nucleation. Xi et al. [15] studied the foam injection molding of isotactic polypropylene/nano-$CaCO_3$ composites, evaluating the effects of the processing conditions on the microstructures of microcells, including filler weight content, mold temperature and injection speed. A 3D model was implemented to analyze the process using a commercial simulation software. The simulated results of bubble morphology, compared to the experimental ones, pointed out a good agreement with the flow field, bubble nucleation and bubble growth. Han et al. [16,17] implemented a numerical model into commercial software which computed the bubble nucleation and growth after validating the simulation results with the viscosity measurement and molding experiments. A good agreement was achieved between the numerical and experimental comparison.

The analysis of the above literature survey makes it evident that a deep knowledge of material properties is very important in polymeric foam processing. However, an integrated and well-structured approach was not proposed. For this reason, the objectives of this paper were the analysis of a polymer blend and the evaluation of its processability with foam injection molding, with the aim of establishing a standard testing cycle for the evaluation of new matrix material by using a numerical-experimental approach. This cycle started with the formulation of the polymeric blend and measurements of its main thermal and rheological material properties to identify the main processing parameter window. The numerical simulation of flow behavior allowed the computation of the final microstructure of the foamed part. The processability of the blend in real conditions was assessed by measuring the real manufactured microstructure and then through the evaluation of the mechanical behavior of the foamed parts in terms of stress-strain curves comparing results in a selected range of process conditions. The proposed framework could be not only interesting for research but also highly demanded by industrial companies working in this field.

Examination procedure

The generation of bubbles within a liquid, creating gas/liquid interfaces, was the main aspect in common to all the foaming techniques investigated. In our case, the foams were obtained by the addition of a chemical blowing agent such as an organic compound with a low molecular weight, mixed with the polymeric blend. Bubble formation is not a spontaneous process and a lot of energy is needed to create a foam from a liquid, according to Drenckhan and Saint-Jalmes [18]. The interactions between material, process and properties are decidedly complex. The examination procedure adopted to deal with this complexity was thus realized in four main phases (Fig. 1), those necessary to characterize the virgin materials, simulate the mold filling, produce a foam part and test its mechanical response. Detailed instructions on how to set-up, execute and evaluate a test case were defined for each phase. The detailed instructions also specified the sequence of actions needed to manufacture the test parts. In this way, the influence of the material properties on part performance was correctly assessed.

The material characterization was conducted using Differential Scanning Calorimetry (DSC) and Rotational Rheometry. A DSC 403 F3 Pegasus (Netzsch-Gerätebau GmbH, Selb, Germany), equipped with a Rhodium Furnace (sensor type S) and a DSC head (sensor types E) was used. The main processing factors of the DSC analysis were the thermal cycle as well as the heating and cooling rates. Each thermal cycle consisted of two consecutive runs with a heating step from 25 to 250 °C, a holding step for 10 min to erase the thermal history and a cooling step from 250 to 25 °C. All measurements were carried out in the non-isothermal mode with a heating and cooling rate of 10 °C/min, using nitrogen (50 ml/min) as the purge gas. The sample weight of the material in a closed aluminum pan ranged between 6 and 7 mg. The results of the DSC analysis were the determination of the main polymer thermal properties such as the melting and crystallization temperature peaks.

A HAAKE MARS III (Thermo Fisher Scientific Inc, Waltham, USA) in a plate-plate configuration (diameter equal to 25 mm) under nitrogen atmosphere (60 ml/min) was used for the viscosity measurements. The device was equipped with two electrically heated plates and Pyrex glass at the outer enclosure to guarantee a good temperature homogenization in the chamber. The main processing factors of the rotational rheometric analysis were the amplitude, frequency and temperature. Amplitude sweep tests were initially performed to identify a stable linear viscoelastic region of the material. Frequency sweep tests were then carried out to measure the polymer viscosity, selecting a specific set temperature. The result of the analysis with the rotational rheometer was the identification of the Newtonian plateau of the polymer at the selected temperature. The zero-shear viscosity η_0 at low shear rates is an important material property and is directly proportional to the average molar mass. Regression methods were then used to compute the infinite-shear viscosity η_∞ in a shear range in which all the molecules are totally disentangled and oriented.

After the material characterization, parts were manufactured. A chemical foaming agent was added to the plastic materials to be processed just like colorants or other additives. The mixing with the plastic granules was carried out in an automatic blending unit directly on top of the injection molding machine. Two cylinders with the same volume but different diameter to length ratios were produced, identified as type A ($\varnothing 100 \times 40\ mm^3$) and type B ($\varnothing 78{,}5 \times 98\ mm^3$). The two parts were simultaneously produced in a two-cavity mold with a double hot runner system, to guarantee the same processing conditions. The injection molding process

Table 1
DSC results.

Name	Material type	Density (g/cm^3)	Melt temperature (°C)	Cryst. temperature (°C)
Escorene Ultra UL02528CC	EVA (25% VA)	0.951	56.4	51.6
LD 600 BA	LDPE	0.924	108.1	93.1
LD 654	LDPE	0.913	101.3	86.6
HMA 035	HDPE	0.964	145.6	114.7
ADC	ADC	0.550	173.4	90.5

*This data was experimentally obtained by the author.

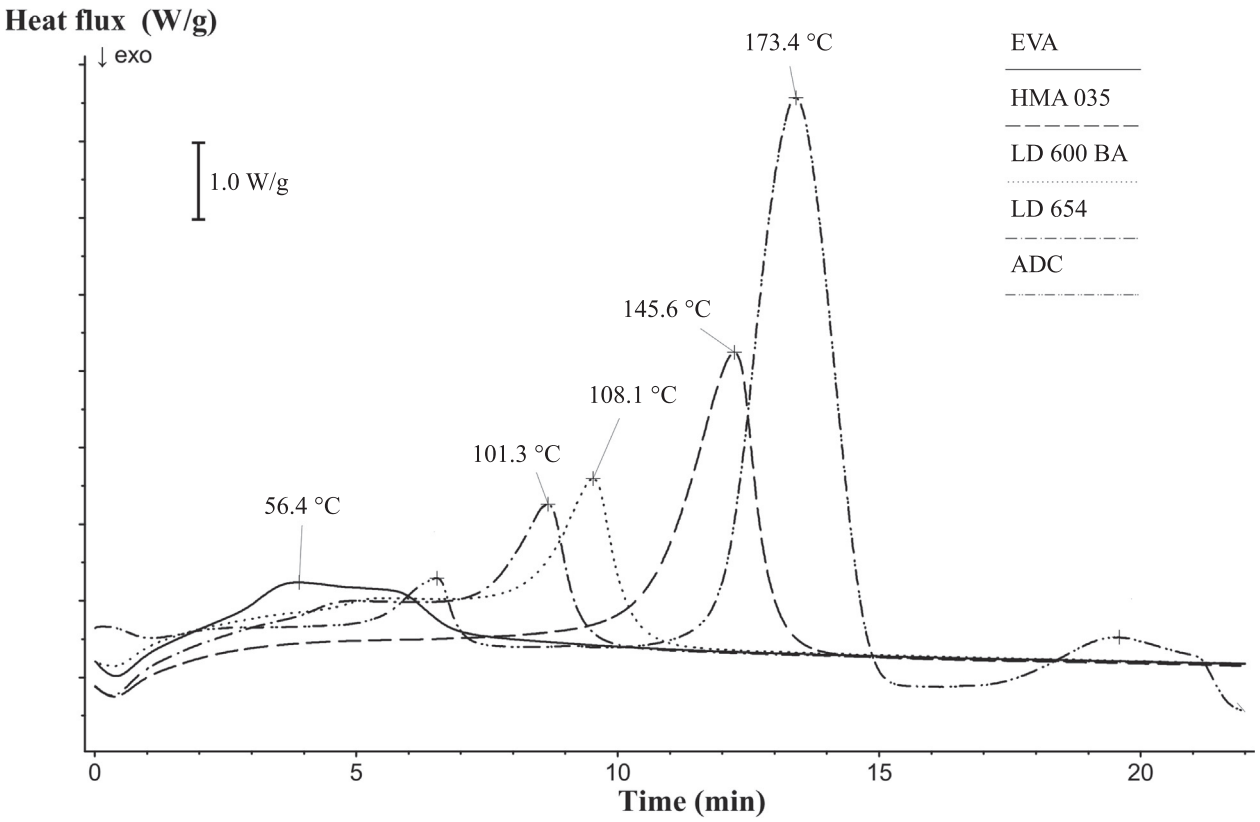

Fig. 2. DSC curves – heating step.

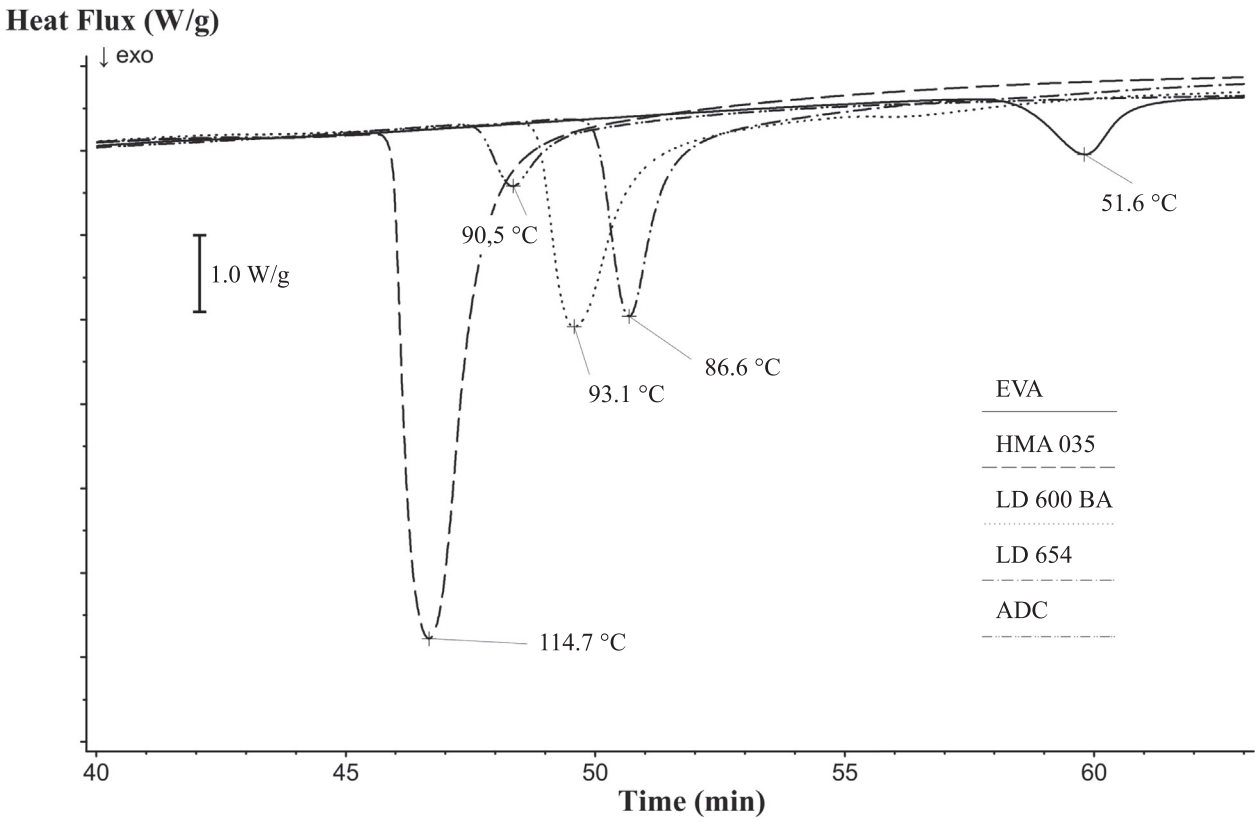

Fig. 3. DSC curves – cooling step.

Table 2
Rheometer results.

Name	Material type	Density (g/cm^3)	Melt flow Index (g/10 min)	Newtonian plateau (Pa × s)
Escorene Ultra UL02528CC	EVA (25% VA)	0.951	25	590.4
LD 600 BA	LDPE	0.924	21	607.6
LD 654	LDPE	0.913	70	199.4
HMA 035	HDPE	0.964	8	1,320.0
ADC	ADC	0.550		

*This data was experimentally obtained by the author.

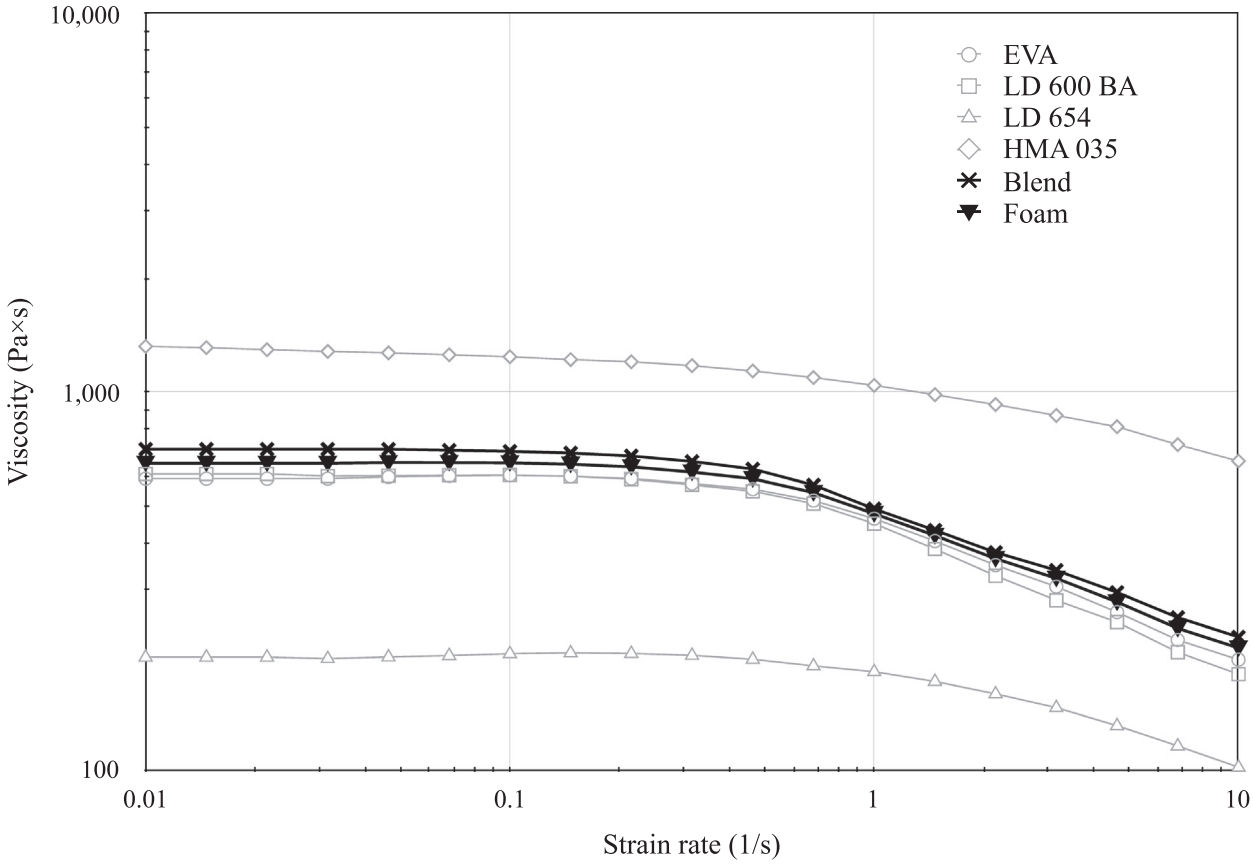

Fig. 4. Viscosity measurements.

was realized on a specialized 60-ton rotary machine (Roto F15E) with 15 stations (Presma SpA, Varese, Italy), equipped with a 62-mm diameter screw (L/D ratio equal to 21) and a special injection system. The injection molding machine also used an efficient shut-off nozzle, a control system of the melt pressure during holding and an injection system with a high-pressure nitrogen booster. A delay time between two consecutive shots was used to avoid polymer expansion in the sprue. The cooling time was a function of the delay time and carousel rotation. Compared to a traditional foam injection machine with a single mold system, the process lead time of this multi-station system is significantly reduced. The investigated processing factors of this manufacturing process were the material volume to be injected and the holding pressure. The variation of these two parameters was sufficient to produce foamed parts with different densities.

Product testing was based on uniaxial compression tests to evaluate the material behavior under crushing loads. The test generally consisted of three cycles with a preload and load release to stabilize the material, followed by the main cycle in which the force-displacement curve was measured and recorded. This procedure was necessary to reduce the Mullins effect, as reported by Krishnaswamy and Beatty [19]. All compression tests were carried-out at room temperature.

Analysis of the material properties

The virgin materials were low-density polyethylenes (LDPEs) named LD 600 BA and LD 654, a high-density polyethylene (HDPE) named HMA 035, an ethylene-vinyl acetate (EVA) and an azodicarbonamide (ADC). The commercially available injection molding grades of LDPEs, HDPE and EVA were supplied by ExxonMobil Chemical (Irving, TX, United States) whereas the ADC was supplied by Rifra Mastebatches SpA (Molinetto di Mazzano, BS, Italy). The main result of the DSC analysis was the determination of the melting and crystallization temperature peaks of the polymers and decomposition temperatures of the foaming agent, as reported in Table 1. These data were extracted from the curves recorded during the thermal cycle of the DSC apparatus in non-isothermal mode with heating and cooling rates equal to 10 °C/min, shown in Figs. 2 and 3. More details can be found in Spina [20].

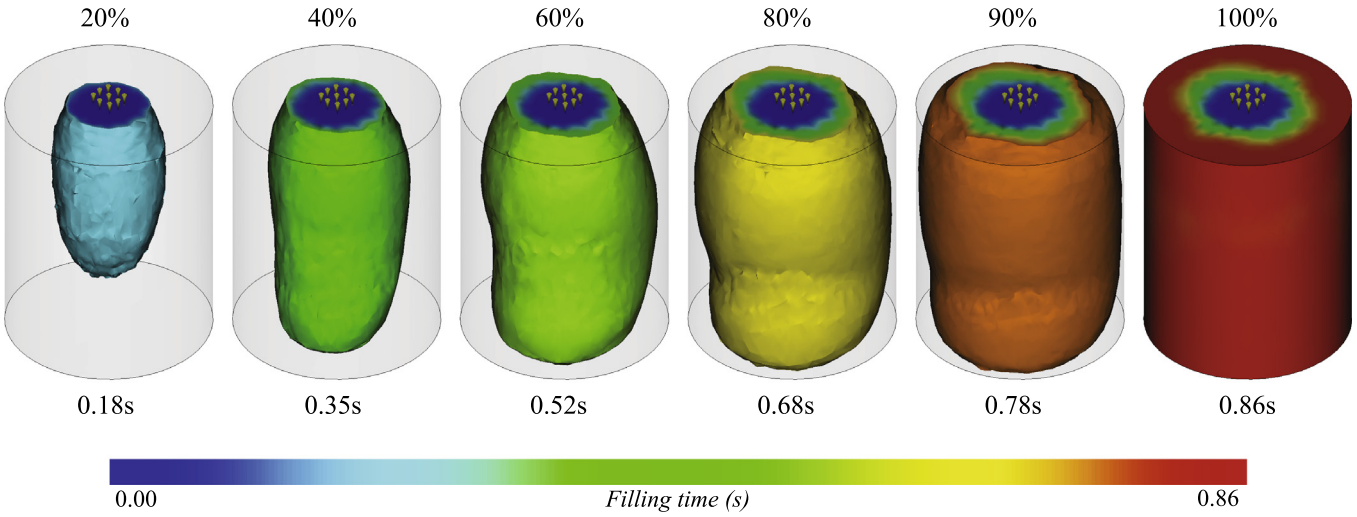

Fig. 5. Flow front advancement/solid part.

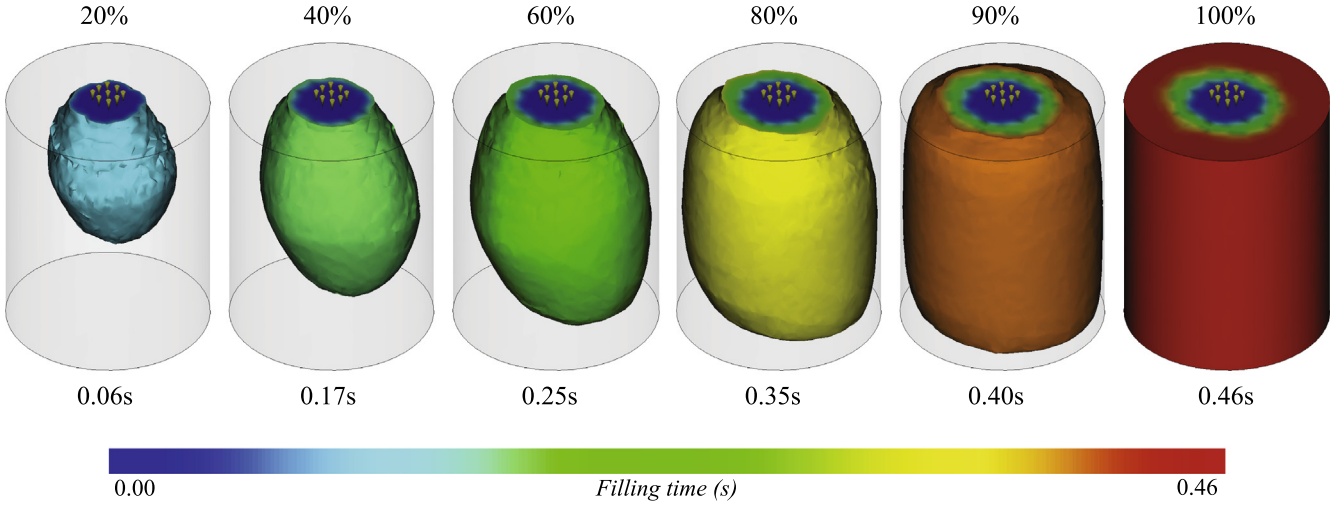

Fig. 6. Flow front advancement/Foamed part.

Table 3
Numerical parameters.

Name	Value
Mold temperature	40 °C
Injection temperature	220 °C
Fill/holding switch	10 mm
Holding time	2 s
Cooling time	40 s
Weight of CBA	2%

The melting peak of EVA was very broad, remaining quite constant in the range 50–80 °C and with a small peak at 56.4 °C. The melting peaks of PEs were a function of the material density because the higher the density, the higher was the melting peak value. The main melting peak of the ADC was detected at 173.4 °C. Two secondary peaks were identified for a lower and a higher temperature. This latter peak revealed that some residues remained and an additional stage could be needed to eliminate them (Sauceau et al. [21]). Concerning the crystallization temperatures, the same trend as for the melting temperature was recognized with the highest crystallization temperature associated to the HDPE (114.7 °C), followed by the LDPEs (93.1 and 86.6 °C) and EVA (51.6 °C). A small crystallization peak of the ADC was also detected at 90.5 °C. This peak was associated to a final stage of the decomposition of the ADC. Based on the DSC results, the compound made up of all the virgin materials to form a mechanical mix could be processed at 200 °C, achieving the complete melting of the mix and the activation of the foaming agent during the injection molding process.

The following analysis was conducted on the rotational rheometer with the aim of identifying the Newtonian plateaus of the polymers and comparing these values with the melt flow indexes declared by the supplier. The measurements were carried out with a strain value of 5% and at a temperature of 200 °C. The viscosities were measured and plotted as a function of strain rate in the range between 10^{-2} and 10 1/s. Table 2 contains the results of the rheometer analysis and Fig. 4 the viscosity curves of the virgin materials.

The viscosities of the EVA and LDPE LD 600 BA were similar, with the Newtonian plateaus equal to 590.4 and 607.6 Pa × s. The viscosities of HDPE and LDPE LD 654 were higher and lower respectively. The next step was the characterization of the blend. The first aspect to deal with was the shear segregation necessary to attain a homogeneous mixture. A low-viscosity polymer in the blend acted as a lubricant in the high-shear rate regions of the injection molding screw, where viscous dissipation should be maximized. This caused a decrease in the energy available to melt the

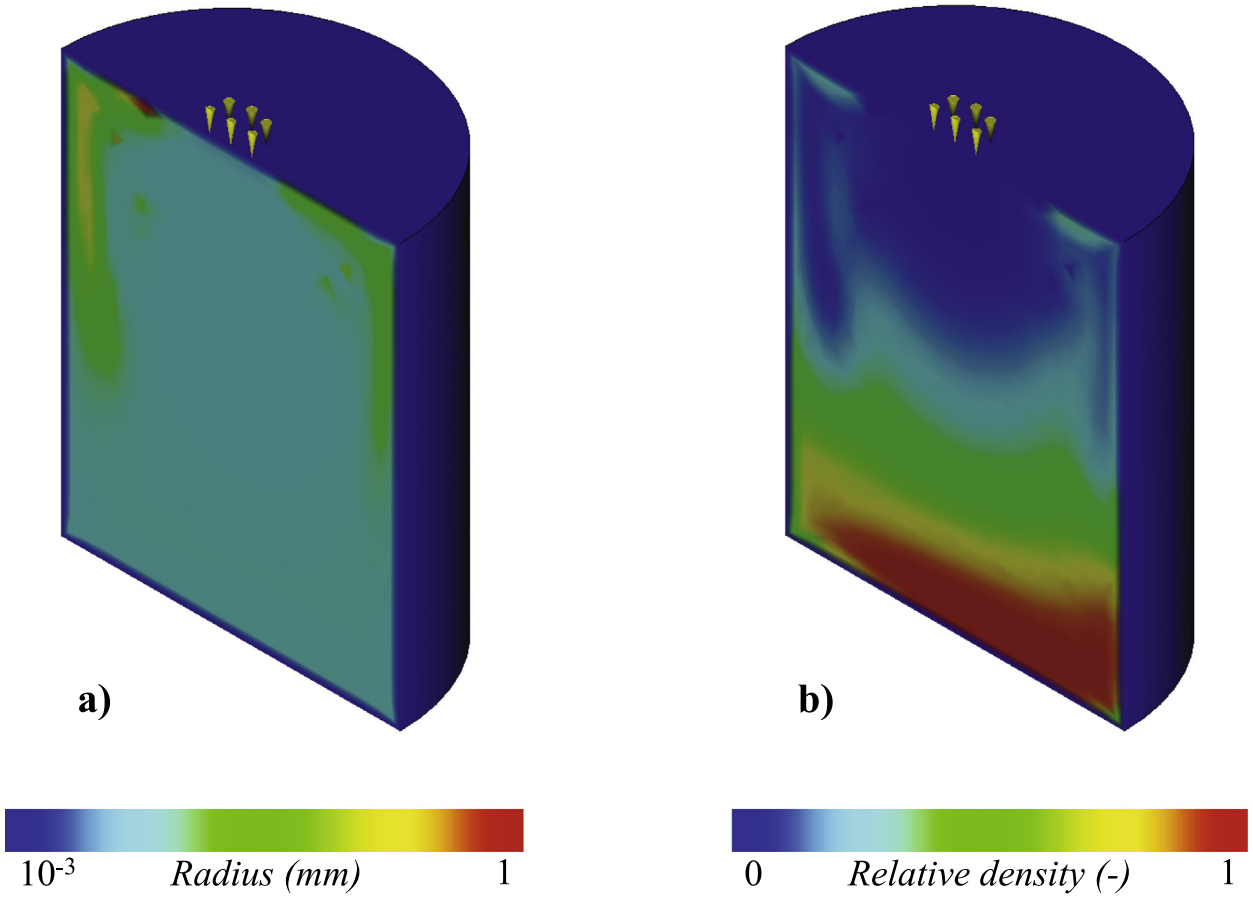

Fig. 7. Bubble radius and density.

high-viscosity polymers and a decrease in the rate of mixing (see Burch and Scott [22]). For this reason, a mechanical mix with a weight percentage of virgin materials equal to 70/20/10 (LDPE/EVA/HDPE) was made up with the objective of achieving flow characteristics similar to EVA. The viscosity of the mix was thus slightly higher than EVA, with a Newtonian plateau equal to 706.2 Pa × s. This viscosity value was used as a reference because the presence of gas generated by ADC reduce the blend viscosity, thus allowing the blend to be manufactured at lower temperatures and pressures, as reported by Areerat et al. [23]. This advantage was important for EVA because of its thermal sensitivity in a narrow processing window. The viscosity of the foam was lower than that of the blend, with a Newtonian plateau equal to 648.3 Pa × s, due to the presence of bubbles. Based on the above results of the material characterization, the most appropriate injection temperature was set to 200 °C to achieve the best mixing and homogenization of the blend polymers and a good viscosity, avoiding the thermal degradation of the low melt components. An increase in this melt temperature reduced the melt viscosity, resulting in lower injection pressure. The melt viscosity reduction also caused a lowering of the rate of gas expansion inside the foam cells, which were cooled and solidified, thus preventing cell rupture. However, this did not simply imply that a higher melt temperature would be always beneficial for the foaming process (see Klempner and Sendijarevic [24]).

Numerical simulations

A numerical model of the part flow analysis was implemented by using Moldflow MPI (Autodesk Inc, CA, United States). The conservation equations of mass, momentum and energy were used:

$$\frac{\partial \rho}{\partial t} + \nabla \cdot (\rho \underline{u}) = 0 \tag{1}$$

$$\rho\left(\frac{\partial \underline{u}}{\partial t} + \underline{u} \cdot \nabla \underline{u}\right) = -\nabla p + \nabla \cdot \underline{\underline{\tau}} + \rho \underline{g} \tag{2}$$

$$\rho c_p\left(\frac{\partial T}{\partial t} + \underline{u} \cdot \nabla T\right) = \nabla \cdot (k \nabla T) + \underline{\underline{\tau}} : \nabla \underline{u} + \beta T\left(\frac{\partial p}{\partial t} + \underline{u} \cdot \nabla p\right) \tag{3}$$

where ρ is the foam density, $\underline{u}$ the velocity vector, p the pressure, $\underline{\underline{\tau}}$ the stress tensor, $\underline{g}$ the gravity vector, c_p the specific heat, T the temperature, k is the heat conduction and β the coefficient of volume expansion. The stress tensor $\underline{\underline{\tau}}$ was related to the viscosity η of the foam through the Stokes stress constitutive equation

$$\underline{\underline{\tau}} = \eta \cdot [(\nabla \underline{u}) + (\nabla \underline{u})^T] \tag{4}$$

$$\eta = \eta_{blend}(1 - \varphi)^{V_1} exp(V_2 c + V_3 c^2) \tag{5}$$

where η_{blemd} is the viscosity of the blend with no bubbles inside, φ the volume fraction of the bubbles, c the gas concentration and V_1, V_2 and V_3 data-fitted coefficients.

Cell nucleation and growth models (Han et al. [16,17]) were coupled to the conservation equations of mass, momentum and energy to predict the pressure and temperature fields, as well as the bubble growth behavior during the process. The main assumptions of the model were related to the bubble formation and growth, namely: i) the chemical reaction generating the foaming gas was complete and fully occurred in the barrel, ii) all by-products of the chemical reaction were ignored, and iii) no chemical kinetics equations for gas generation were solved. The main effects of these assumptions were to speed up the simulation com-

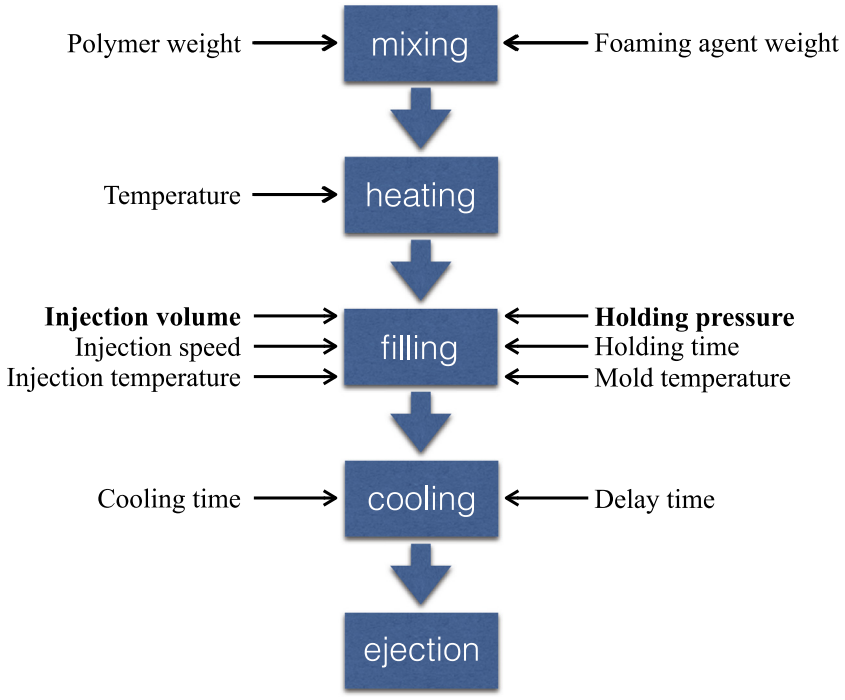

Fig. 8. Process flow.

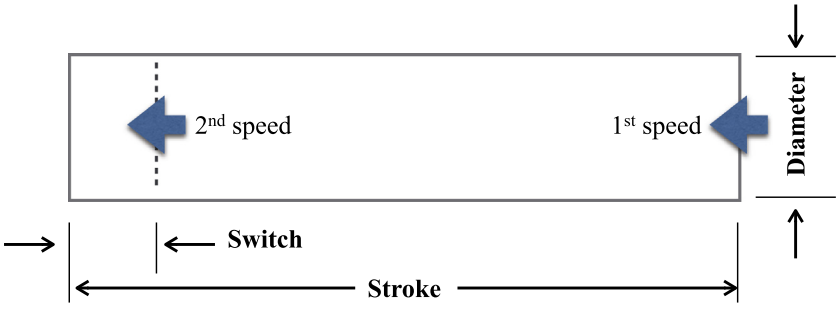

Fig. 9. Shot volume.

Table 4
Injection molding results.

Part ID	Injection volume		Holding pressure	Weight		Density	Simulated Density
	Stroke (mm)	Switch (mm)	(MPa)	Type A (g)	Type B (g)	(g/cm^3)	(g/cm^3)
1 – 45/5/5	45	5	5	93.7	93.6	0.201	0.205
2 – 50/5/5	50	5	5	96.8	96.7	0.208	0.214
3 – 55/5/5	55	5	5	100.1	100.2	0.216	0.220
4 – 60/5/5	60	5	5	115.9	115.9	0.249	0.249
5 – 60/10/5	60	10	5	115.8	115.8	0.249	0.251
6 – 60/15/5	60	15	5	115.6	115.7	0.249	0.254
7 – 55/10/5	55	10	5	104.8	104.4	0.225	0.220
8 – 50/5/8	50	5	8	98.9	98.6	0.212	0.220
9 – 50/5/7	50	5	7	97.3	97.8	0.210	0.215
10 – 50/5/6	50	5	6	96.6	96.5	0.208	0.209

putation, focusing on flow front advancement rather than chemical solving, avoiding describing the bubble growth accurately for only a few seconds with a huge amount of the computations per second, according to Elshereef et al. [25]. The equation of the bubble nucleation rate is based on the classical nucleation theory, as formulated by the following equation:

$$J = f_0 \left(\frac{2\gamma}{\pi \frac{M_w}{N_a}} \right)^{0.5} exp\left[-\frac{16\pi\gamma^3 F}{3k_B T (p_b - p_a)^2} \right] \quad (6)$$

where f_0 and F are fitting parameters, γ the surface tension, M_w the molecular weight of the chemical blowing agent, N_a the Avogadro's

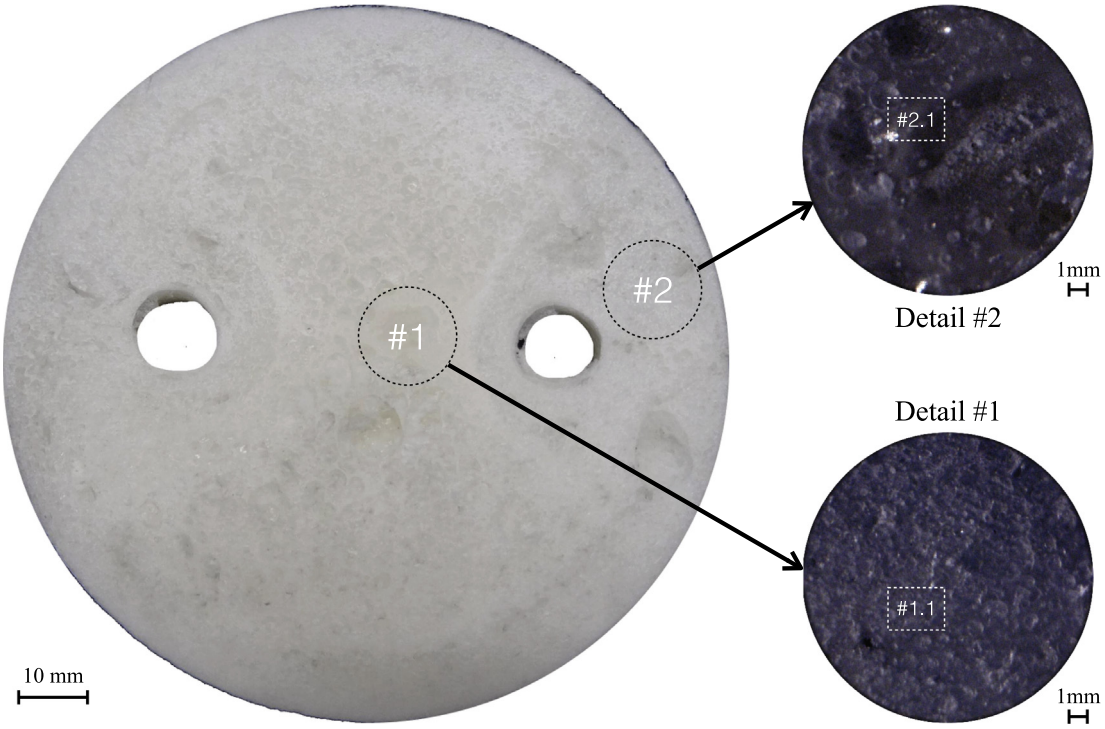

Fig. 10. Part section – type A.

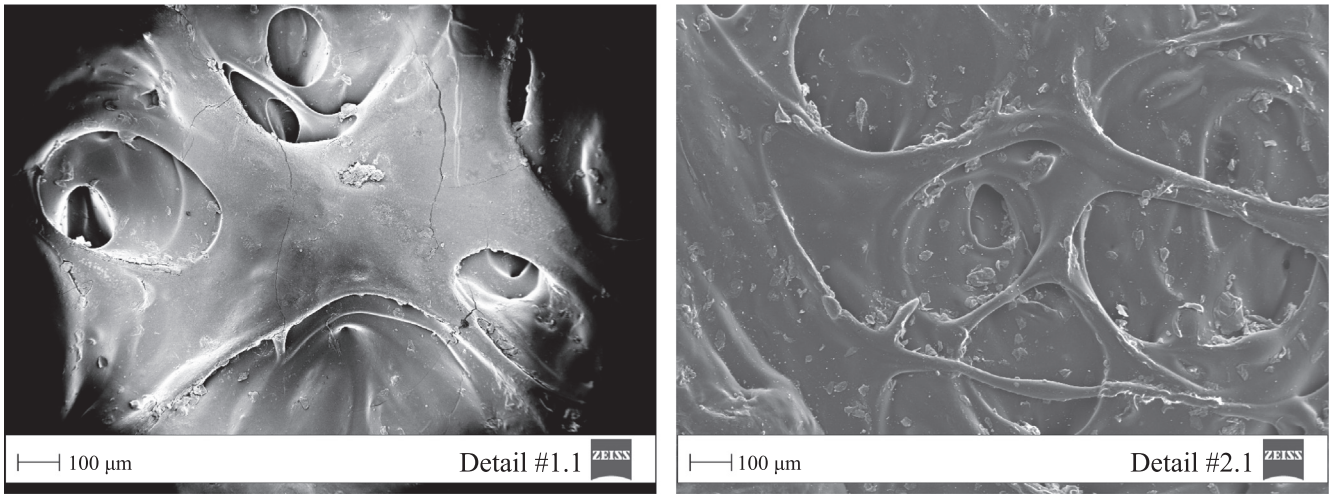

Fig. 11. SEM analysis.

number, k_B the Boltzmann's constant, p_b and p_a the bubble and ambient pressure. The variation of the bubble radius r over time is:

$$\frac{dr}{dt} = \frac{r}{4\eta}\left(p_b - p_a - \frac{2\gamma}{r}\right) \tag{7}$$

coupled to the equation of the bubble pressure distribution during molding:

$$\frac{d}{dt}\left(\frac{p_b r^3}{RT}\right) = 6\rho^2 D k_H RT \frac{(p_{b,0} - p_b)^2 r^4}{p_b r^3 - p_{b,0} r_0^3} \tag{8}$$

where R is the gas constant, k_H the diffusivity, $p_{b,0}$ and r_0 the initial bubble pressure and radius.

A 3D model of the type B specimen was designed, consisting of more than 300,000 tetrahedra to capture the polymer flow during filling as well as the variation in density between the core and surface of the part. The mold filling, as predicted from numerical simulations, is shown in Figs. 5 and 6 for standard and foam injection molding respectively, using parameters reported in Table 3. The first part of the mold to fill out is shown in blue whereas the last part to be filled is shown in red.

The cavity filling and packing characteristics of the foam injection molded part were quite different from those of the standard injection molded part. In fact, the process was essentially a "*short-shot*" process because filling and packing were provided by cell growth rather than by movement of the injection screw (see Berry [26]). The flow front was quite radial near the gate and mainly linear along the cylinder axis for both cases, with a net projection to the surface opposite the injection side because the part was thick. The molten polymer filled up the free space after reach-

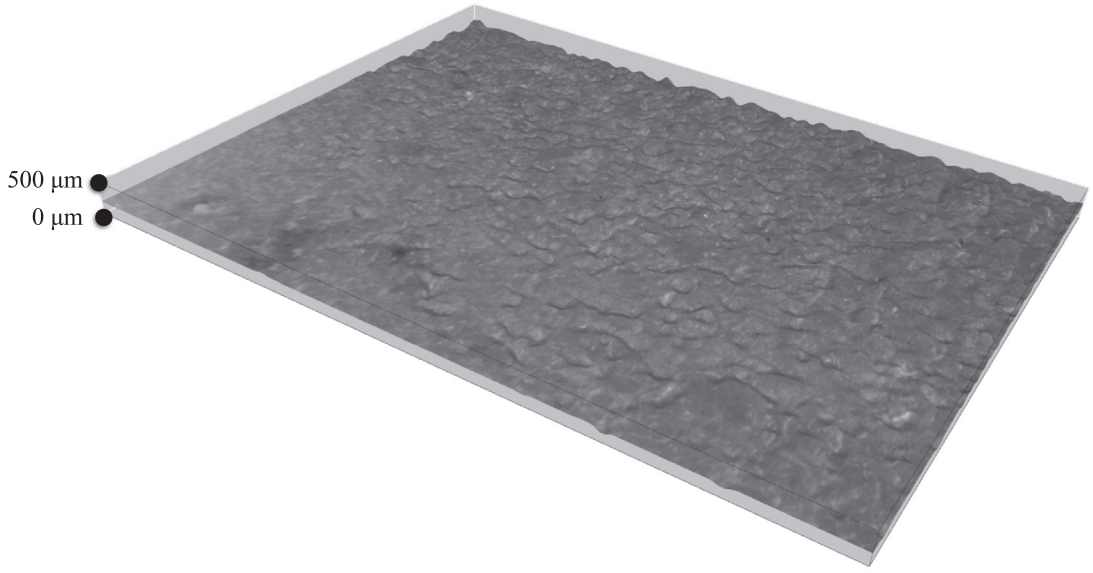

Fig. 12. Scanned surface.

ing the surface opposite to the gate, filling all the gaps between the polymer and the mold. The effect of the gas was to expand the flow front advancement in the radial direction already in the initial steps, pushing the molten polymer plastic to enlarge its area during cavity filling. For this reason, a stable blend viscosity over the processing temperature range was more suitable to obtain the best results. No surface blistering, in terms of tiny bubbles on the part surface, was detected during the numerical simulations, pointing out that the process parameters were correctly selected. The filling time of the foamed part was approximately half than that of the solid part because of the lower melt viscosity. The final density of the foamed part was about 0.201 g/cm^3. The foam morphology of plastic had an important influence on the mechanical properties. The morphology is normally characterized by the pore density, in terms of the number of pores per area, and the average pore diameter. The non-homogeneity of the density and the foam structure made the characterization complex, especially when several sections exist (Kirschling [27]). The thickness of the skin layer and the average pore diameter were important values to characterize the foamed part. The average pore diameter was mainly determined by the amount of blowing agent, considering that the higher the amount of blowing agent, the larger was the nucleation in the polymer melt. Fig. 7 reports the results of bubble radius and relative density of the foamed part. The size of the bubbles, distributed throughout the part, was useful to evaluate the process efficiency as well as the skin thickness. Smaller bubble radius was normally located at the surface of the part with a higher radius at the center of the part. The relative density of bubbles was a function of the normalized number of bubbles distributed throughout the part. This value was dependent on the nature and volume of the foaming gas, polymer properties, local temperature and pressure. Ideally, the bubble number density should be fairly uniform throughout the core regions of the part. An area with very few bubbles may indicate an insufficient presence of the foaming gas or a rapid cooling of the part that limited the pressure decreased for a correct bubble growth.

Evaluation of the injection foamed parts

Once the materials had been characterized and simulation runs completed, the manufacturing process started. The two injection-molding parameters selected as variables for this study were the injection volume (*VOL*) and holding pressure (*HOLD*). This choice was made according to the research findings of Gómez-Gómez et al. [28]. The other parameters, shown in Fig. 8, were kept constant.

The mechanical mix was conveyed, plasticized, homogenized, metered and injected by the plastification unit, using an increasing linear profile of barrel temperature. The different values of the injection volume were achieved by setting the starting and switch points of the plastification unit stroke and the associated high and low values of the injection speed. The change between the high and low injection speeds occurred at the switch point (see Fig. 9).

The cooling and delay times were set to guarantee a good surface finishing on the molded parts. During the injection processing, there was a strict correlation between process parameters and the quality of product produced (Hassan [29]). Tests were repeated 3 times after 10 processing runs to stabilize the machine conditions after changing the process parameters, thus avoiding improper settings of process parameters inducing defects in the products. The diameter, height and weight of each specimens were measured. Table 4 summarizes the details of the tests carried out on types A and B samples, compared with the numerical results of the FE simulations on part type B. The average measurements of three consecutive runs, respectively identified by the triplet *ID-A*/*B*/*C* in the ID column of the table, are also reported. *A*, *B* and *C* stand for stroke, switch and holding pressure respectively. The foam density ρ was simply computed as the mean ratio between the part weight and its shot volume, according to the following formula:

$$\rho = \frac{4 \cdot W_{mea}}{\pi \cdot H_{mea} \cdot D_{mea}^2} \tag{9}$$

where W_{mea}, D_{mea} and H_{mea} are the measured weight, diameter and height of a part respectively. The nominal density of the unformed blend ρ_{blend} of the material from which the foam was made, was equal to 0.930 g/cm^3. The absolute average deviation between experimental and numerical results was about 8%.

The results of the injection molding process, supported by the numerical results, led to some preliminary considerations. The first was that minor differences in part weight of the two part types were detected for the same shot. The second consideration was related to the influence of the main parameters on the part weight.

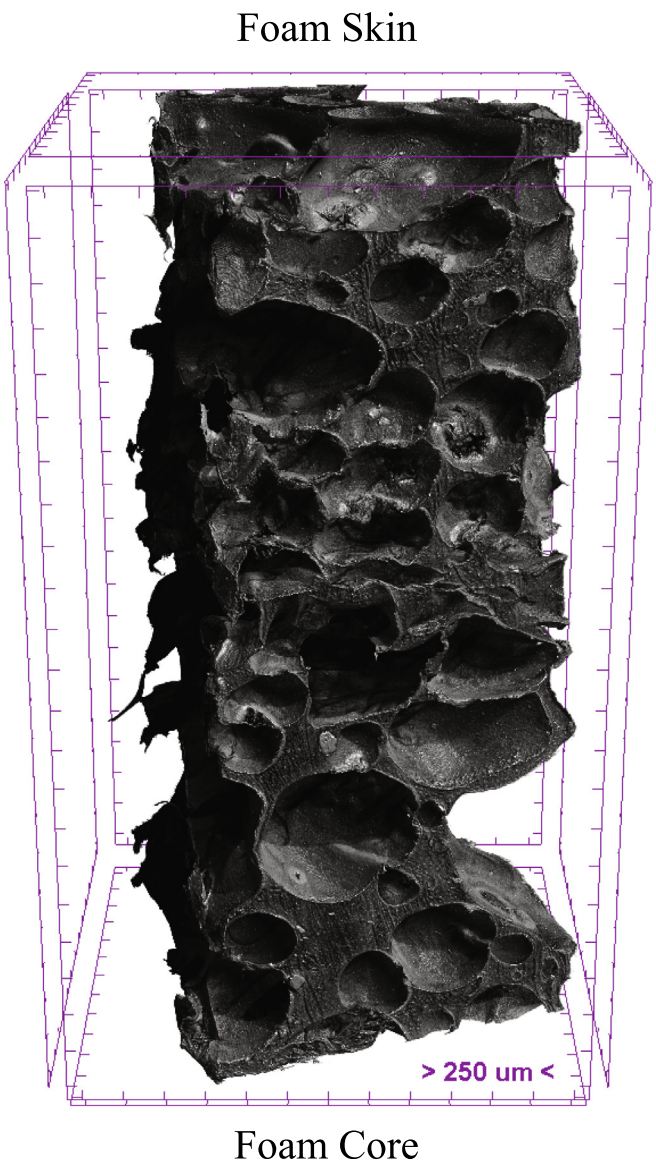

Fig. 13. Micro-CT analysis.

An increase in the shot volume *VOL* and holding pressure *HOLD* caused both an increase in the part weight and density (Table 4). However, the influence of the shot volume was more important than that of the holding pressure.

The first evaluation of the injection molding process was performed by analyzing several cuts of a foamed part using a multipurpose zoom microscope system AZ100M (Nikon Instruments Europe BV, Amsterdam, Netherlands). The circular cross-sections were obtained by using a diamond cut-off wheel and grinding with several SiC foils (grit size FEPA P from 120 to 4000). Fig. 10 shows one of these sections extracted from a type A specimen, characterized by a well formed cellular core (Detail #1) and a lower porous area near the external contours (Detail #2). The analysis was then extended to higher magnification with a combine field emission scanning electron microscope (FE-SEM) SIGMA300 (Carl Zeiss Microscopy, Jena, Germany), as Fig. 11 shows. Detail #1.1 is extracted from the core of the specimen whereas Detail #2.2 from the part skin. A closed-cell structure was typical of this foam, independently of the location of the observation area. The cells were not spherical since deformation occurred in the flow direction due to shear and elongation stresses but an ellipsoid shape was detected. However, it is important to underline that a random slicing was performed and this inevitably led to the underestimation of the true cell size.

The external surface was accurately examined to identify specific defects caused by gas formation, such as the presence of small bubbles on the external surfaces of the part. These defects were not detected in any production run, pointing out the stability of the process. These results overcome the limitation of the chemical agent decomposition, normally characterized by a limited control of porosity that can lead to a product with a non-uniform cellular structure. A 3 D representation of Detail #1 was realized by selecting the in-focus area from several images with different focal points, and producing one all-in-focus image (Fig. 12). It is possible to note that the surface porosity was equally distributed. This analysis was extended to higher magnification by using a high-resolution micro computed tomography SKYSCAN1272 (Bruker, Billerica, MA, USA). In this way, the cell structure was not influenced by the slicing method. The close cell structure with ellipsoid shape of the cells was also revealed with this analysis. The porosity was approximately 330 μm, with a standard deviation of approximately 150 μm (Fig. 13).

One of the main findings of this approach, not explored in this research activity, was the possibility to further use the micro-CT volumes to perform the structural analysis of foams to optimize the product and production process. In this way, a better understanding of the numerical correlation between the structure and physical properties of foams could be achieved.

Mechanical tests were then performed on the manufactured parts. It is important to underline that an accurate description of the mechanical behavior of polymer blend is needed to predict the warpage of injection-molded parts, according to Sun et al. [30]. Compression testing under uniaxial loads between two parallel plates allowed the basic deformation mechanisms of specimens to be recorded and the behavior under static conditions to be studied. The main result was the analysis and comparison of the stress-strain curves of the two part types. Tests were carried-out on a servo-controlled 4485 machine (Instron, Norwood, USA). The load and displacement accuracies were 0.25% with a 200 kN load cell and 2.5×10^{-5} mm. The initial compression deformation rates of the part types A and B were 4×10^{-2} and 5×10^{-2} 1/s, corresponding to crosshead speeds of 2.0 and 5.0 mm/s respectively, following the testing protocol of Briody et al. [31]. A 0.5 N preload was applied to each specimen prior to the test. The measured stress-strain curves, reported in Fig. 14 for type B specimen (identified with ID1-45/5/5), showed three different zones: the first zone from origin O to P_1 in which the material behavior was linearly elastic; the second zone from P_1 to P_2 (plateau) with a long plateau of roughly constant stress, and finally the third region from P_2 to P_3 in which the material showed a rapid stress increase due to the remarkable increase in density of the material. The same figure shows some snapshots captured during testing at some specific points of the stress-strain curve. The central section initially collapsed at the end of the linear zone, associated to P_1. This collapse involved the adjacent sections with a strain increase until P_2 and the complete specimen height at P_3. At the end of the test, the specimen was fully folded. The load was then released, using the same crosshead speed adopted during the test, and the specimen almost recovered its initial height.

The compression test was repeated for the type A specimen and the results compared with those for the type B specimen. Some important differences in the stress-strain curve of the type A specimen were recorded, as shown in Fig. 15.

The yield point becomes less obvious as the foam density decreases. Probably due to the lower height of the part that prevented the collapse in the central section, the linear elastic zone of the type A specimen had a lower slope whereas the plateau

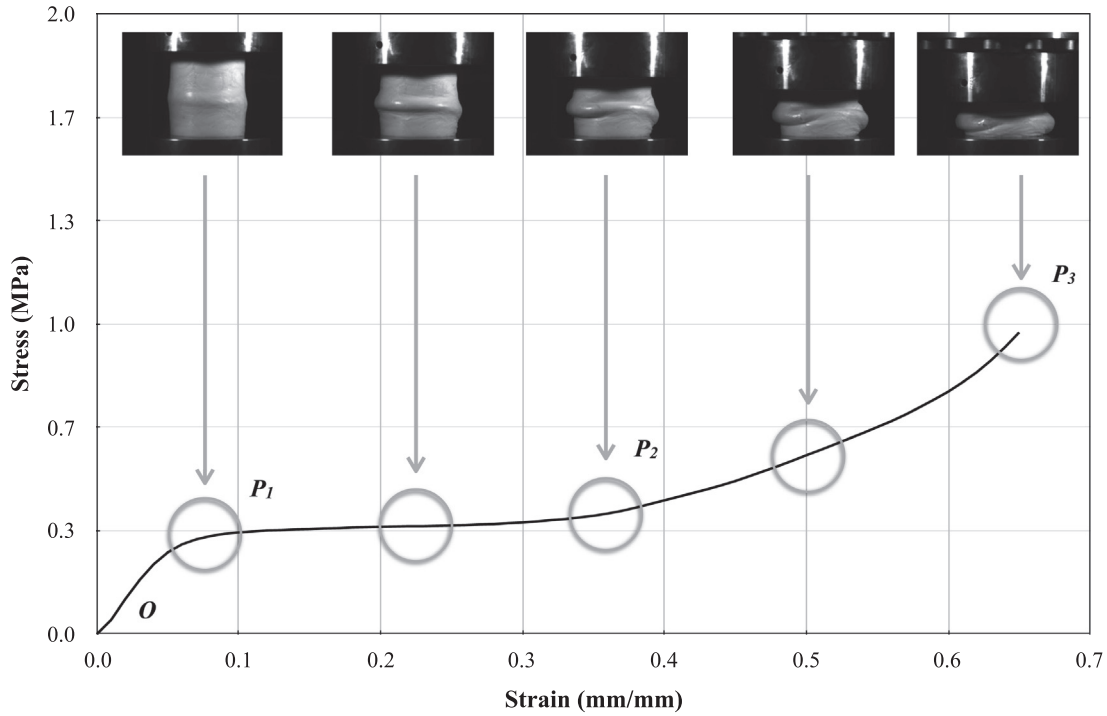

Fig. 14. Stress-strain curve of type B specimen.

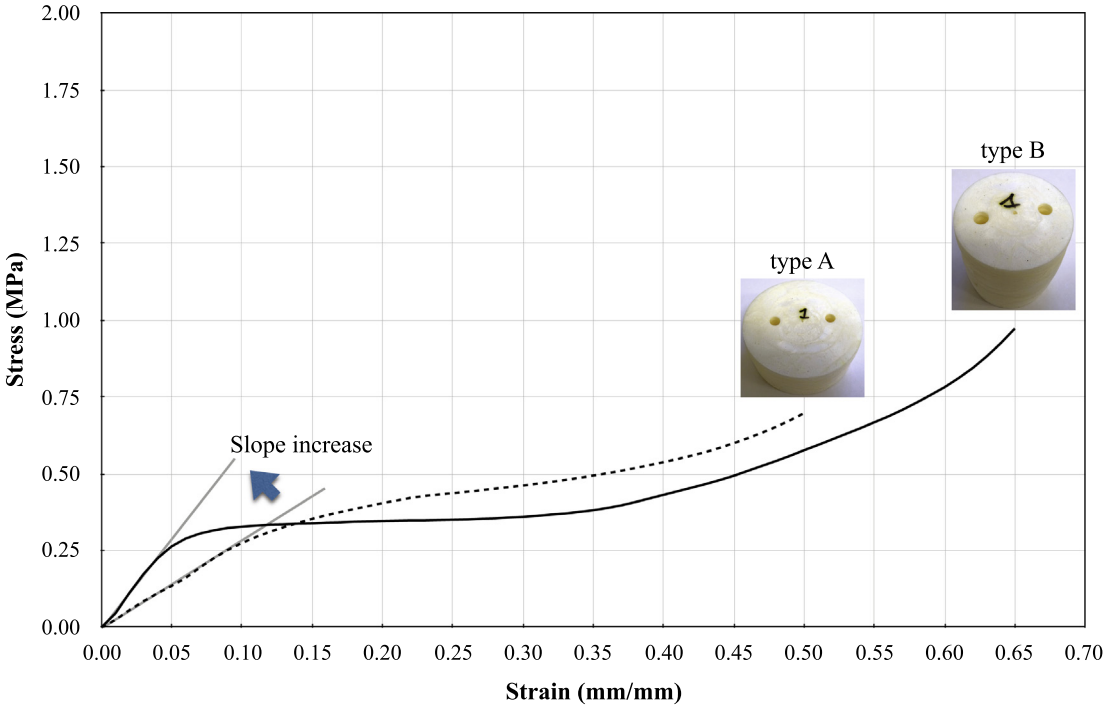

Fig. 15. Stress-strain curves of types A and B specimens.

slope was higher. On the contrary, the deformation mechanism of the type B specimen, caused by a non-uniform deformation in the central section, led to a decrease in the apparent elastic modulus with an increase in strain in the plateau stress regime, as described by Flores-Johnson et al. [32]. Similar stress-strain curves were registered for the other specimens, as shown in Figs. 16 and 17.

The comparison between specimen ID3-55/5/5 and ID8-50/5/8 was interesting, for both types A and B. The ID3-55/5/5 specimens were manufactured with an intermediate value of the shot volume and the lowest holding pressure whereas the ID8-50/5/8 specimens were realized with a lower value of the shot volume but the highest value of the packing pressure. The ID3-55/5/5 and ID8-50/5/8 specimens had nearly equal densities and their stress-strain curves were very similar. For this reason, it was more convenient to change the specimen density by varying the shot volume rather than the holding pressure. The importance of the

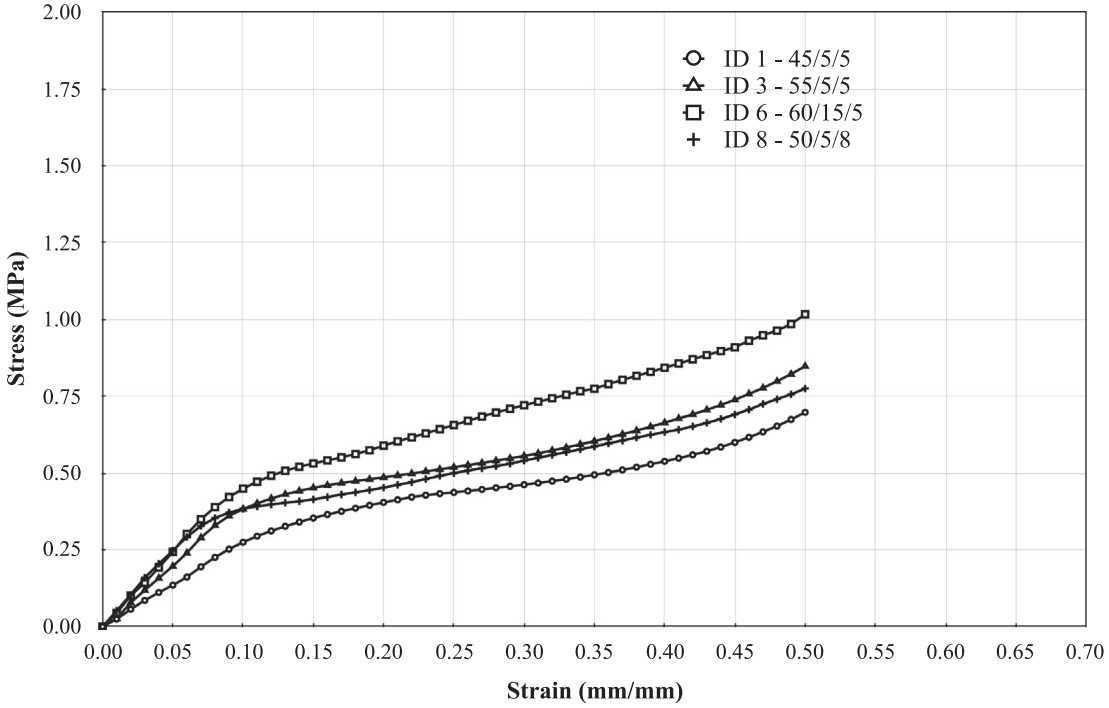

Fig. 16. Stress-strain curves of type A specimens.

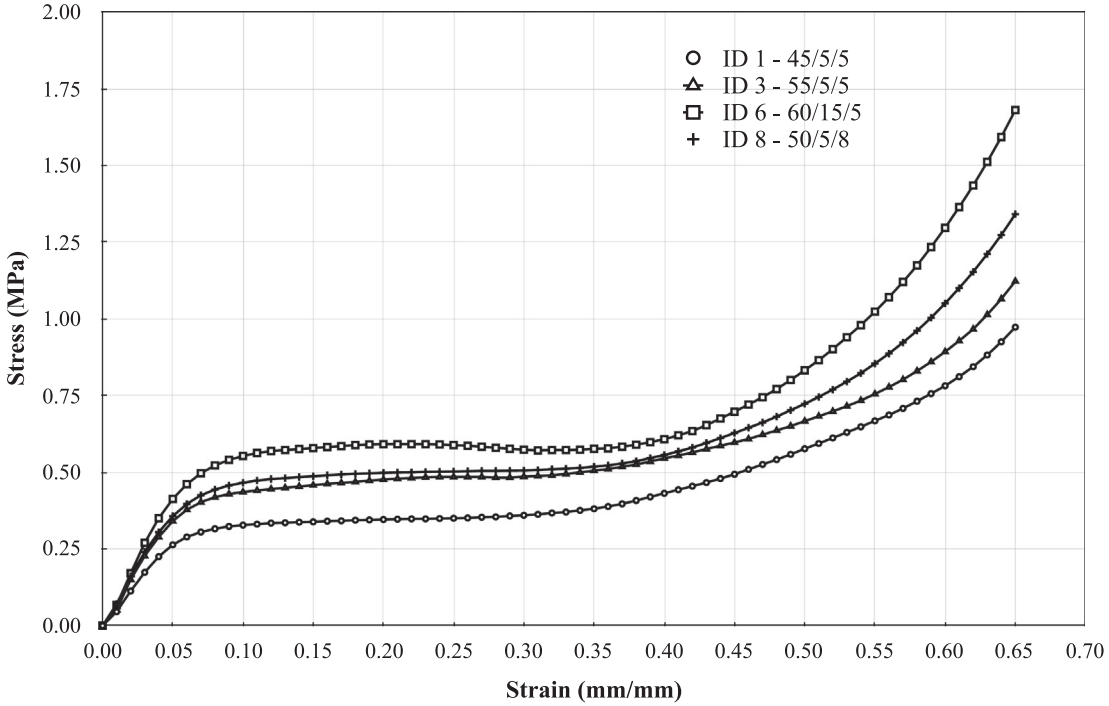

Fig. 17. Stress-strain curves of type B specimens.

improvement in density was validated by ID6-60/15/5 specimens, which presented the highest density value and consequently the highest stress-strain curve. This behavior may be validated according to notes of Gibson and Ashby [33]. They explained that at lower density, the densification zone was reached quickly, which resulted in a very high force prior to full energy dissipation. On the other hand, in the case of high-density foam, the force exceeded the critical value before adequate energy absorption, resulting in partially utilized compression strains. The analysis of the stress-strain curves was extended to all specimens. The extraction of the tensile test results was performed according to Mirfendereski et al. [34] and the main parameters are reported in Table 5.

The elastic modulus *E* was computed as the slope of the linear region O-P_1, the plateau was the slope in the region between P_1 and P_2, whereas the *UTS* was computed as the maximum stress value at a specific strain (0.50 and 0.65 for types A and B respec-

Table 5
Compression test results.

Part ID	Density (g/cm^3)	Relative density (−)	Type A			Type B		
			Elastic (MPa)	Plateau (Mpa)	UTS (MPa)	Elastic (MPa)	Plateau (Mpa)	UTS (MPa)
1 – 45/5/5	0.201	0.223	2.678	0.646	0.697	5.635	0.122	0.973
2 – 50/5/5	0.208	0.230	3.605	0.707	0.685	6.552	0.141	1.230
3 – 55/5/5	0.216	0.239	4.119	0.754	0.848	7.586	0.150	1.123
4 – 60/5/5	0.249	0.276	4.993	1.260	1.008	8.747	0.203	1.653
5 – 60/10/5	0.249	0.276	4.991	1.258	1.005	8.752	0.207	1.625
6 – 60/15/5	0.249	0.276	4.987	1.265	1.016	8.758	0.208	1.680
7 – 55/10/5	0.225	0.249	4.623	1.003	0.921	7.997	0.174	1.347
8 – 50/5/8	0.212	0.235	4.032	0.829	0.775	7.511	0.138	1.341
9 – 50/5/7	0.210	0.233	3.559	0.784	0.772	7.103	0.135	1.318
10 – 50/5/6	0.208	0.230	3.614	0.713	0.677	6.552	0.142	1.230

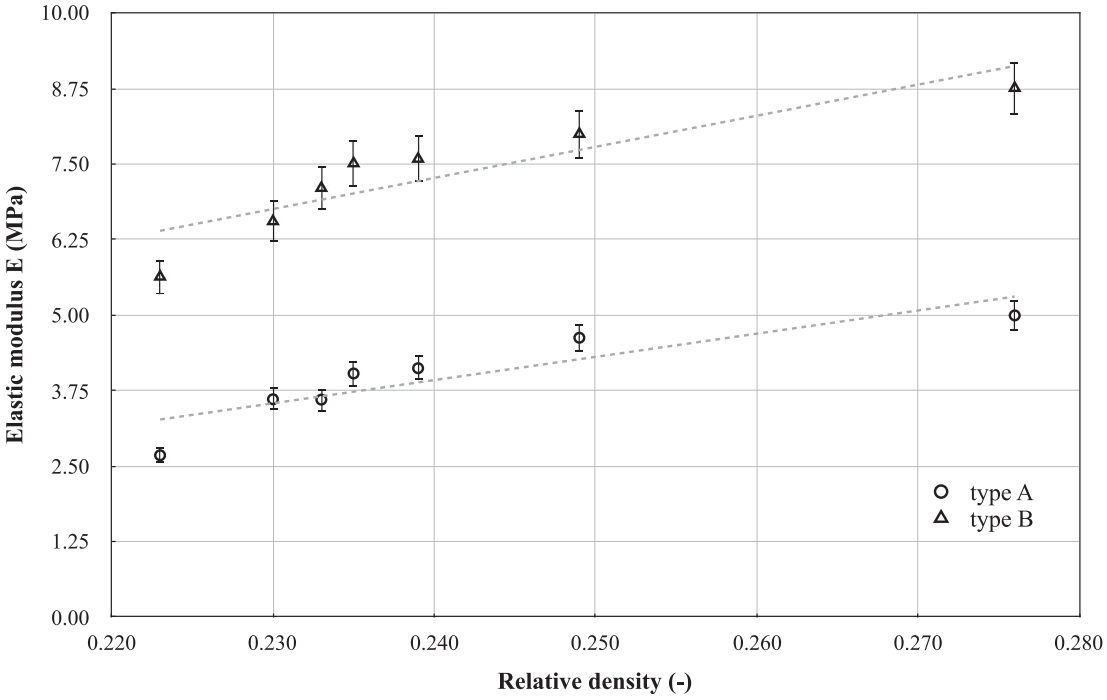

Fig. 18. Elastic modulus.

tively). The results are reported as a function of the density. Specimens with the lowest density values were characterized by the lowest mechanical strength in terms of elastic modulus *E* and ultimate tensile strength *UTS*, independently of the part type. On the contrary, the highest mechanical strength was associated to the highest density value.

An attempt was made to determine the relationship between *E* and *UTS* with foam density through the best fitting of the experimental data using a power function (dotted curves in the plots of Figs. 18 and 19). Foam mechanical properties, as a function of the relative density ρ_{foam}/ρ_{blend}, are often explained using a simplified micro-structural model built from cubic cells, as reported by Rodríguez-Perez [35]. The relative density was the most important structural characteristic of a foamed plastic. The effects of foam density on mechanical properties are expressed in terms of the relative density, using the following equations:

$$E = C_E \cdot \left(\frac{\rho_{foam}}{\rho_{blend}}\right)^{\eta_E} \tag{10}$$

$$UTS = C_{UTS} \cdot \left(\frac{\rho_{foam}}{\rho_{blend}}\right)^{\eta_{UTS}} \tag{11}$$

with data fitted coefficients C_E, C_{UTS}, n_E and n_{UTS}, reported in Table 6. The same predictions could be carried-out by substituting the experimental results with the numerical computations, defining material parameters for the following structural analysis.

Conclusions

A structured approach has been implemented to study the behavior of the PE/EVA polymeric foam blend both numerically and experimentally. The numerical simulation of the foaming injection process computed the filling stage and predicted the material behavior by providing using useful suggestions before mechanical testing was performed. The main results are the identification of a proper process parameter window for foaming injection molding. The flow front advancements of un-foamed and foamed blend were computed as well as the part density, consequently allowing the evaluation of the effects on mechanical characterization. The research has overcome limitations related to the fact that most of the work performed was related to a single foam without considering the finer implications on the property and modeling of the blend. The temperature was found to be the main influencing factor through the DSC and rheological analyses while

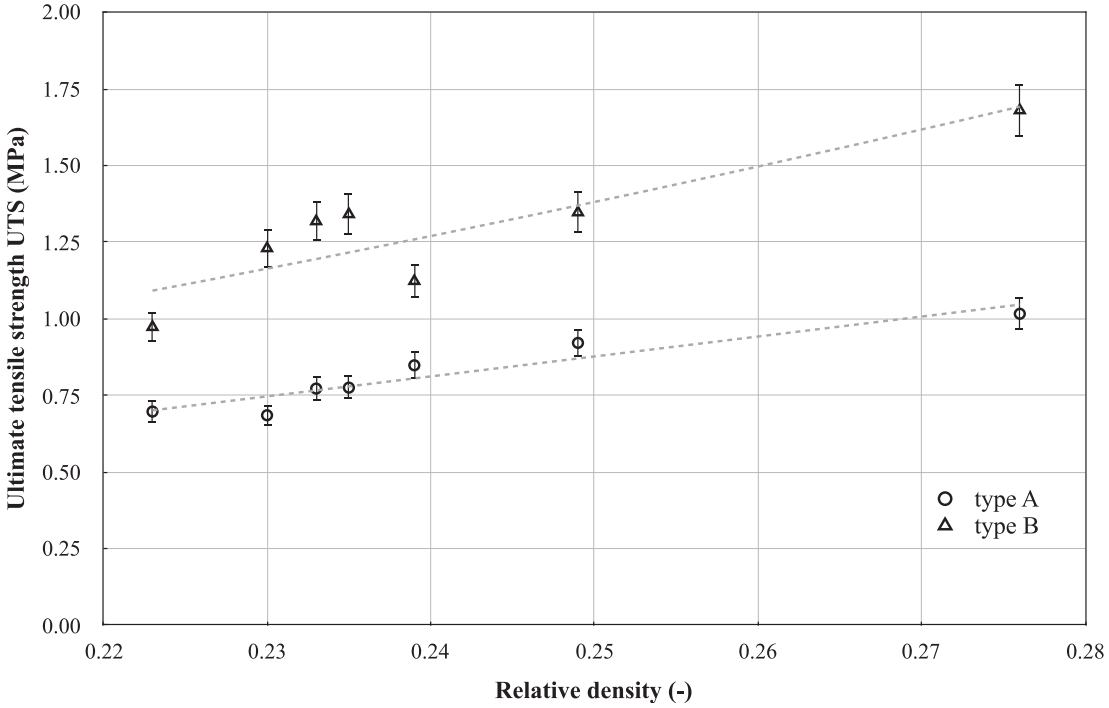

Fig. 19. Ultimate tensile strength.

Table 6
Data fitted coefficients.

Part type	C_E (MPa)	n_E (−)	C_{UTS} (MPa)	n_{UTS} (−)
A	92.35	1.785	12.651	1.928
B	135.06	2.488	23.824	2.055

the shot volume was identified after compression tests on foamed products. Further research will be addressed to include the structural analysis in the framework, starting from the foma model of the micro-CT results.

Acknowledgment

The author wishes to acknowledge and thank Prof. Luigi Tricarico (DMMM - Politecnico di Bari) and Alfredo Vania (Vanplast srl) for their precious support during the research activities. The author acknowledges funding for this work from the Italian National Operative Program as a SMATI project (PON01_02584).

References

[1] Notario B, Pinto J, Rodríguez-Perez MA. Towards a new generation of polymeric foams: PMMA nanocellular foams with enhanced physical properties. Polymer 2015;63:116–26.
[2] Cappetti N, Donnarumma A, Naddeo A, Russo L. Design of experiment about foam CF45 for pedestrian safety in car design. J Mater Process Technol 2006;175:77–82.
[3] Yousef BF, Murad A-BI, Hilal-Alnaqbi. Modeling of the mechanical behavior of polyethylene/polypropylene blends using artificial neural networks. Int J Adv Manuf Technol 2013;64:601–11.
[4] Demir H, Sipahioglu M, Balko D, Ulku S. Effect of additives on flexible PVC foam formation. J Mater Process Technol 2008;195:144–53.
[5] Pantani R, Volpe V, Titomanlio G. Foam injection molding of poly(lactic acid) with environmentally friendly physical blowing agents. J Mater Process Technol 2014;214:3098–107.
[6] Kim Y, Park CB, Chen P, Thompson RB. Maximal cell density predictions for compressible polymer foams. Polymer 2013;54:841–5.
[7] Arencon D, Antunes M, Realinho V, Velasco JI. Influence of chemical nature, expansion ratio and cellular morphology on the fracture behavior of flexible polyolefin-based foams assessed by the Essential Work of Fracture (EWF). Polym Test 2015;43:163–72.
[8] Kossa A. A new biaxial compression fixture for polymeric foams. Poly Test 2015:45–51.
[9] Chinesta F, Cueto E, Quintela P, Paredes J. Induced anisotropy in foams forming processes: modelling and simulation. J Mater Process Technol 2004;155–156:1482–8.
[10] Maheo L, Viot P. Impact on multi-layered polypropylene foams. Int J Impact Eng 2013;53:84–93.
[11] Banyay GA, Shaltout MM, Tiwari H, Mehta BV. Polymer and composite foam for hydrogen storage application. J Mater Process Technol 2007;14:102–5.
[12] Zhang L, Zhao G, Wang G. Formation mechanism of porous structure in plastic parts injected by microcellular injection molding technology with variable mold temperature. Appl Therm Eng 2017;114:484–97.
[13] Aloku GO, Yuan X-F. Numerical simulation of polymer foaming process in extrusion flow. Chem Eng Sci 2010;65:3749–61.
[14] Taki K. Experimental and numerical studies on the effects of pressure release rate on number density of bubbles and bubble growth in a polymeric foaming process. Chem Eng Sci 2008;63:3643–53.
[15] Xi Z, Chen J, Liu T, Zhao L, Turng LS. Experiment and simulation of foaming injection molding of polypropylene/nano-calcium carbonate composites by supercritical carbon dioxide. Chin J Chem Eng 2016;24:180–9.
[16] Han S, Costa F, Klompen E. Analysis of the foam injection molding process using a chemical blowing agent. SPE ANTEC Indianalolis; 2016.
[17] Han S, Costa F, Kishbaugh L. Numerical and experimental studies on bubble nucleation and growth during microcellular injection molding. SPE ANTEC Orlando; 2015.
[18] Drenckhan W, Saint-Jalmes A. The science of foaming. Adv Colloid Interface Sci 2015;222:228–59.
[19] Krishnaswamy S, Beatty MF. The Mullins effect in compressible solids. Int J Eng Sci 2000;38:1397–414.
[20] Spina R. Technological characterization of PE/EVA blends for foam injection molding. Mater Des 2015;84:64–71.
[21] Sauceau M, Fages J, Common A, Nicotine C, Rodier E. New challenges in polymer foaming: a review of extrusion processes assisted by supercritical carbon dioxide. Prog Polym Sci 2011;36:749–66.
[22] Burch HE, Scott CE. Effect of viscosity ratio on structure evolution in miscible polymer blends. Polymer 2001;42:7313–25.
[23] Areerat S, Nagata T, Ohshima M. Measurement and prediction of LDPE/CO_2 solution viscosity. Polym Eng Sci 2002;42:2234–45.
[24] Klempner D, Sendijarevic V. Polymeric Foams and Foam Technology. Hanser Fachbuchverlag; 2004.

[25] Elshereef R, Vlachopoulos J, Elkamel A. Comparison and analysis of bubble growth and foam formation models. Eng Computation 2010;27:387–408.
[26] Berry M. Microcellura injection molding, Applied Plastics Engineering Handbook. William Andrew Pub.; 2011. 215-226.
[27] Kirschling HMM. Mikroschäume aus Polycarbonat, Herstellung – Struktur – Eigenschaften Dissertation, PPH ZAPOL Dmochowski, Sobczyk Spo´łka Jawna: Kassel; 2009.
[28] Gómez-Gómez JF, Arencón D, Sánchez-Soto MA, Martínez AB. Influence of the injection-molding parameters on the cellular structure and thermo-mechanical properties of ethylene-propylene block copolymer foams. Adv Polym Tech 2013;32E:692–704.
[29] Hassan H. An experimental work on the effect of injection molding parameters on the cavity pressure and product weight. Int J Adv Manuf Technol 2012;67:675–86.
[30] Sun X, Su X, Mao J, Tibbenham P, Tao J, Bao Z. The application of modified viscoplastic constitutive relationship on the warpage prediction of injection-molded part. Int J Adv Manuf Technol 2016. http://dx.doi.org/10.1007/s00170-016-8390-1.
[31] Briody C, Duignan B, Jerrams S, Tiernan J. The implementation of a visco-hyperelastic numerical material model for simulating the behavior of polymer foam materials. Comput Mater Sci 2012;64:47–51.
[32] Flores-Johnson EA, Li QM, Mines RAW. Degradation of elastic modulus of progressively crushable foams in uniaxial compression. J Cell Plast 2008;44:415–34.
[33] Gibson LJ, Ashby MF. Cellular solids: structures and properties. 2nd ed. Cambridge: Cambridge University Press; 1997.
[34] Mirfendereski L, Salimi M, Ziaei-Rad S. Parametric study and numerical analysis of empty and foam-filled thin-walled tubes under static and dynamic loadings. Int J Mech Sci 2008;50:1042–57.
[35] Rodríguez-Perez MA. Crosslinked polyolefin foams: production, structure, properties, and applications. Adv Polym Sci 2005;184:97–126.